

Polyoxometalates-Modulated Hydrophilic-Hydrophobic Composite Interfacial Material for Efficient Solar Water Evaporation and Salt Harvesting in High Salinity Brine

Sihang Cheng¹, Cuimei Liu¹, Yingqi Li¹, Huaqiao Tan¹, Yonghui Wang¹, and Yangguang Li¹

¹Northeast Normal University

February 8, 2023

Abstract

Solar vapour generation (SVG) represents a promising technique for seawater desalination to alleviate the global water crisis and energy shortage. One of its main bottleneck problems is that the evaporation efficiency and stability are limited by salt crystallization under high-salinity brines. Herein, we demonstrate that the 3D porous melamine-foam (MF) wrapped by a type of self-assembling composite materials based on reduced polyoxometalates (i.e. heteropoly blue, HPB), oleic acid (OA) and polypyrrole (PPy) (labeled with MF@HPB-PPy-OA) can serve as efficient and stable SVG material at high-salinity. Structural characterizations of MF@HPB-PPy-OA indicate that both hydrophilic region of HPBs and hydrophobic region of OA co-exist on the surface of composite materials, optimizing the hydrophilic and hydrophobic interfaces of the SVG materials, and fully exerting its functionality for ultrahigh water-evaporation and anti-salt fouling. The optimal MF@HPB-PPy10-OA operates continuously and stably for over 100 h in 10 wt% brine. Furthermore, MF@HPB-PPy10-OA accomplishes complete salt-water separation of 10 wt% brine with 3.3 kg m⁻² h⁻¹ under 1-sun irradiation, yielding salt harvesting efficiency of 96.5%, which belongs to the record-high of high-salinity systems reported so far and reaches zero liquid discharge. Moreover, the low-cost of MF@HPB-PPy10-OA (2.56 \$/m²) suggests its potential application in the practical SVG technique.

DOI: 10.1002/ ((please add manuscript number))

Article type: Research Article

Polyoxometalates-Modulated Hydrophilic-Hydrophobic Composite Interfacial Material for Efficient Solar Water Evaporation and Salt Harvesting in High Salinity Brine

Sihang Cheng, Cuimei Liu, Yingqi Li, Huaqiao Tan*, Yonghui Wang, Yangguang Li*

S. H. Cheng, C. M. Liu, Prof. Y. Q. Li, Prof. H. Q. Tan, Prof. Y. H. Wang and Prof. Y. G. Li

Key Laboratory of Polyoxometalate and Reticular Material Chemistry of Ministry of Education, Faculty of Chemistry, Northeast Normal University, Changchun, 130024, P. R. China

E-mail: tanhq870@nenu.edu.cn; liyg658@nenu.edu.cn

Abstract

Solar vapour generation (SVG) represents a promising technique for seawater desalination to alleviate the global water crisis and energy shortage. One of its main bottleneck problems is that the evaporation efficiency and stability are limited by salt crystallization under high-salinity brines. Herein, we demonstrate that the 3D porous melamine-foam (MF) wrapped by a type of self-assembling composite materials based on reduced polyoxometalates (i.e. heteropoly blue, HPB), oleic acid (OA) and polypyrrole (PPy) (labeled

with MF@HPB-PPy_n-OA) can serve as efficient and stable SVG material at high-salinity. Structural characterizations of MF@HPB-PPy_n-OA indicate that both hydrophilic region of HPBs and hydrophobic region of OA co-exist on the surface of composite materials, optimizing the hydrophilic and hydrophobic interfaces of the SVG materials, and fully exerting its functionality for ultrahigh water-evaporation and anti-salt fouling. The optimal MF@HPB-PPy₁₀-OA operates continuously and stably for over 100 h in 10 wt% brine. Furthermore, MF@HPB-PPy₁₀-OA accomplishes complete salt-water separation of 10 wt% brine with 3.3 kg m⁻²h⁻¹ under 1-sun irradiation, yielding salt harvesting efficiency of 96.5%, which belongs to the record-high of high-salinity systems reported so far and reaches zero liquid discharge. Moreover, the low-cost of MF@HPB-PPy₁₀-OA (2.56 \$/m²) suggests its potential application in the practical SVG technique.

Keywords: polyoxometalates (POM), heteropoly blue (HPB), hydrophilic-hydrophobic interface, solar vapour generation (SVG), salt-water separation

1. Introduction

Solar vapor generation (SVG) technique holds great promise for applications in solving two of the most serious global challenges: the water crisis and energy shortages.^[1-6] The main bottleneck of this technique is the contradiction between high-efficiency water evaporation and salt crystallization, which dramatically restricts the practical application of SVG, especially in the treatment of highly concentrated brine.^[7-11] Owing to the ultra-low diffusivity of salt in water (10⁻⁹ m²s⁻¹, and the diffusivity of water vapor in air is about 10⁻⁵ m²s⁻¹),^[12] the salt inevitably crystallizes and precipitates on the surface of the photothermal material as the water vapor continues to escape rapidly.^[13, 14] This problem severely hinders the light absorption, water transport and water vapor escape in the continuous water evaporation process, significantly degrading the performance of SVG and terminating the operation of the device. Thus, the development of photothermal water evaporation materials with both efficient water evaporation performance and self-cleaning/anti-salt fouling properties is a key issue to drive SVG from the laboratory to large-scale practical applications.

To achieve the above aim, the SVG materials should possess three key properties. One is displaying the excellent solar light capture and photothermal conversion capability. The other is possessing efficient water evaporation pathway. The third one is having suitable hydrophilic-hydrophobic dual interfaces that can improve the anti-salt fouling ability. Recently, a series of reports by Yu et al. have demonstrated that hydrogen bonding or electrostatic interactions between hydrophilic functional groups and water molecules facilitate the evaporation of bulk water as activated water,^[15-23] providing a fast and efficient water evaporation pathway (exceeding the theoretical evaporation rate value of 1.47 kg m⁻²h⁻¹).^[24] Such evaporation process requires less energy than the conventional single-molecule water evaporation that requires breaking the hydrogen bonds between all water molecules. On the other hand, several studies including hydrophilic-hydrophobic janus and biomimetic structures aim to enhance the anti-salt fouling ability of evaporators through hydrophobic modifications.^[7, 25-32] For example, the hydrophobic surface structure designed by Zhu et al. based on natural water lily can effectively inhibit the crystallization of salt on its surface and achieve the complete separation of salt and water. However, the strongly hydrophobic surface weakened the effective contact of water with the photothermal active site and the water activation capacity, which just yielded an evaporation rate of 1.39 kg m⁻²h⁻¹. Therefore, the combination of three properties into one material is obviously a challenging task for exploring efficient, anti-salt fouling and durable SVG evaporators.

Heteropoly blues (HPBs) that possess a classic blue-black color are reduced polyoxometalates (POMs).^[33-39] They exhibit excellent potential applications in the fields of photothermal catalysis and photodynamic therapy based on their broad and high light absorption properties, unique photothermal activity and stability in the solar spectral range.^[40-46] Moreover, the oxygen-rich surface structure of HPBs strongly supports their affinity for water,^[47, 48] exhibiting the potential in the construction of hydrophilic-photothermal evaporation sites. Importantly, the HPBs that hold high-negative charge can be electrostatically self-assembled with cationic polymers to avoid water leaching problems and achieve efficient and stable loading. Further regulation of the surface microenvironment of the functional self-assembled materials is expected to achieve system management and optimization of the surface local hydrophilic-hydrophobic region, offering an effective strategy for constructing hydrophilic-hydrophobic interfacial SVG evaporators.

Given the above considerations, a new type of photothermal water evaporation materials (*abbr.*MF@HPB-PPy_n-OA) were designed and constructed based on the melamine foam (MF) skeleton, which is covered by a hydrophilic-hydrophobic composite interfacial material via a one-step self-assembly of HPB, oleic acid (OA) and polypyrrole (PPy). On the surface of MF@HPB-PPy_n-OA, the hydrophilic regions of HPB and the hydrophobic regions of OA show spatial separation features due to the electrostatic mutual repulsion of HPB and OA molecules. Benefiting from the advantages of the self-assembly strategy and the unique surface structure, the local hydrophilic-hydrophobic interface of this SVG material can be regulated and optimized so as to realize the ultrahigh water evaporation and salt crystallization simultaneously. In a series of MF@HPB-PPy_n-OA, MF@HPB-PPy₁₀-OA exhibits the best SVG performance, yielding 3.3 kg m⁻² h⁻¹ of evaporation rate and 96.5% of salt harvesting efficiency in the complete salt-water separation process of high-salinity (10 wt%) brine at 1 solar irradiation, and realizes zero liquid discharge, which belongs to the record-high of high salinity systems reported so far. Moreover, MF@HPB-PPy₁₀-OA can operate continuously and stably for over 100 h at an ultrahigh evaporation rate of 3.3 kg m⁻² h⁻¹ (corresponding to an energy efficiency of 92.1%) in continuous solar desalination of high-salinity brine (10 wt%), and enables real-time anti-fouling and maintains surface cleanliness. The low cost, excellent mechanical properties and processability of MF@HPB-PPy₁₀-OA in terms of manufacturing exhibit promising prospects for commercial applications.

Results and discussion

2.1 Preparation and structural characterization of 3D MF@HPB-PPy₁₀-OA

The preparation scheme of MF@HPB-PPy_n-OA is shown in Figure 1a. Firstly, a mixed

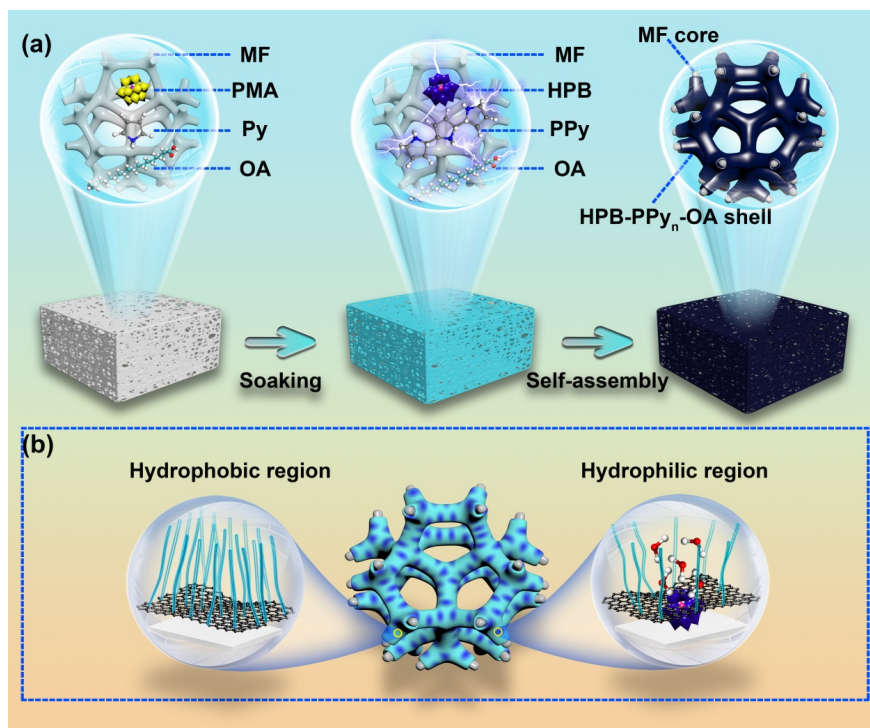


Figure 1. (a) Schematic view of the preparation of 3D MF@HPB-PPy_n-OA by facile one-step self-assembly of H₃PMO₁₂O₄₀·nH₂O (POM), pyrrole (Py) and oleic acid (OA) on melamine foam (MF); (b) On the surface coating of MF@HPB-PPy_n-OA, the hydrophobic regions (left) is mainly occupied by OA molecules, and the hydrophilic regions (right) is mainly composed of HPBs.

ethanol solution containing $\text{H}_3\text{PMO}_{12}\text{O}_{40}\cdot n\text{H}_2\text{O}$ (POM), pyrrole (Py) and oleic acid (OA) is poured on commercially available the melamine foam (MF) that serves as a carrier for self-assembly. In this process, POM is reduced to HPB by triggering the oxidative polymerization of Py to PPy. Then, HPB and OA (acting as electron donors) undergo respectively electrostatic self-assembly with PPy (serving as electron acceptor) on the surface of MF to form a series of hydrophilic-hydrophobic composite interfacial materials (denoted as MF@HPB-PPy_n-OA, n refers to the amount of Py added, n = 5 μL , 10 μL , 20 μL). Influenced by the electrostatic repulsion of HPB and OA, the hydrophilic-hydrophobic units formed by them present distinct spatial separation characteristics on the MF@HPB-PPy_n-OA surface. As shown in Figure 1b, on the surface region without HPB, the PPy surface is modified by OA, forming a hydrophobic region (left). In contrast, the region containing HPBs exhibits affinity to water owing to the absence of OA modification (right). This spatially separated feature implies that the hydrophilic regions of the HPB might form nano water channels for water transport. On one hand, the exposed hydrophilic regions of HPBs enhance the coupling-activation, transport and convection of bulk water under the action of hydrogen bonding or electrostatic forces, thus enhancing the evaporation efficiency of water. On the other hand, the hydrophobic regions endow the 3D porous MF@HPB-PPy_n-OA surface with a powerful anti-salt fouling property. Moreover, salt is also prevented from crystallizing in the hydrophilic regions due to the advantages of the nanoscale dimension of hydrophilic regions and the strong salt-water convection effect between the water channels (It is something like “pits” formed by HPBs with a high salt concentration) and the original microporous channels of MF (with a low salt concentration). The surfacial hydrophilic-hydrophobic dual feature of the porous MF@HPB-PPy_n-OA is further modulated by adjusting the loading different amount of HPBs. Among them, MF@HPB-PPy₁₀-OA stands out in terms of its ability in photothermal water evaporation and anti-salt fouling properties, thus, it is selected as an example for elucidation in detail.

SEM and TEM show the morphology of MF@HPB-PPy₁₀-OA. As shown in Figure 2a and Figure S1, the HPB, PPy, and OA are clearly self-assembled on the smooth skeleton surface of MF (Figure S1a and Figure S1b), forming a HPB-PPy₁₀-OA self-assembled coating. Meanwhile, the resulting MF@HPB-PPy₁₀-OA preserves the original 3D porous structure of MF. TEM further reveals that HPB-PPy₁₀-OA is stacked by irregular lamellar structures (Figure S2b and Figure S2c). In the HR-TEM image (Figure 2b), we observe that the HPB clusters are uniformly dispersed in the amorphous PPy lamellar structures. The uniformity distribution of C, N, O, Mo and P elemental components and the completeness of HPB-PPy₁₀-OA coating coverage are evidenced by TEM-EDX and SEM-EDX mapping analysis (Figure 2c), respectively. Notably, the cross-sectional SEM images (Figure S1e, Figure S1h and Figure S1k) display that the self-assembled layers of MF@HPB-PPy₅-OA, MF@HPB-PPy₁₀-OA and MF@HPB-PPy₂₀-OA became progressively thicker with increasing the proportion of Py substrate in the reaction system. At the same time, the loading of HPB is gradually diminished (Figure S3), implying that the hydrophilic-hydrophobic properties of the surface are controllable. The corresponding water contact angle measurements verify this conclusion (Figure S1f, Figure S1i and Figure S1l). A control sample MF@PPy₁₀-OA without HPB is firstly prepared (see Synthesis 2.1 section for details), and the water contact angle is about $132.0 \pm 3^\circ$, exhibiting a strong hydrophobicity as demonstrated in Figure 2d. When the hydrophilic HPB is introduced, the water contact angle on the surface of the material gradually decreases with the increase of HPB loading, and the corresponding hydrophilicity is

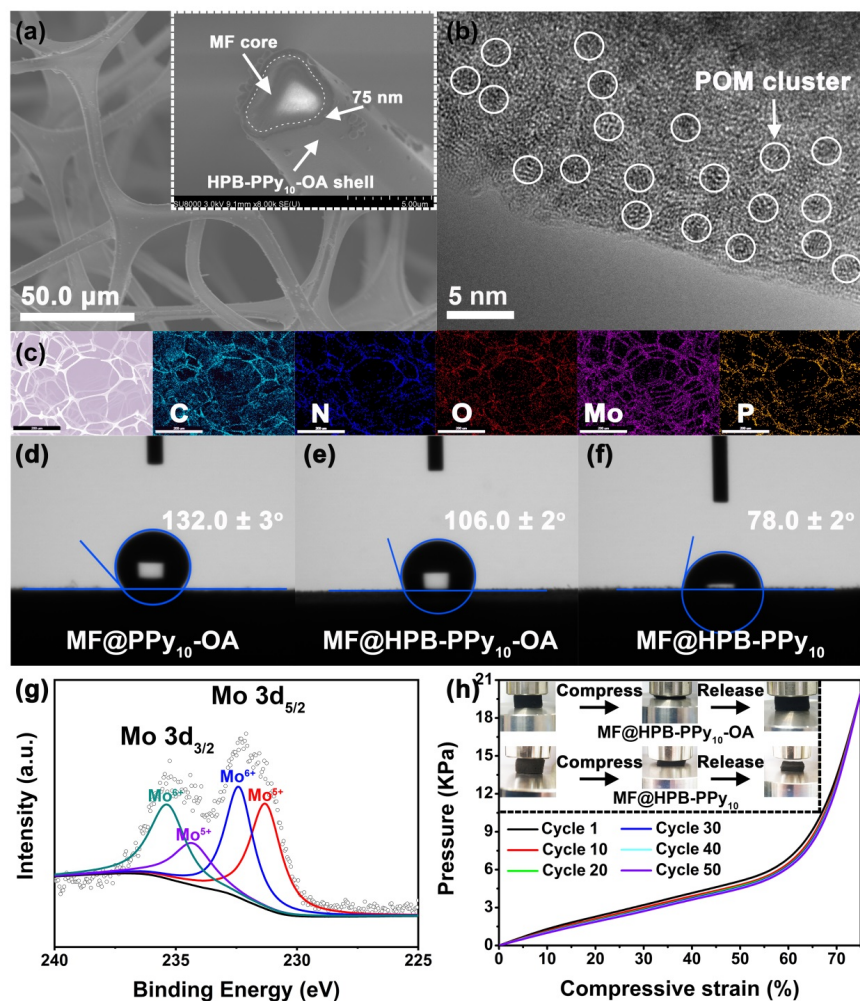


Figure 2. Characterization of the as-prepared MF@HPB-PPy₁₀-OA. (a) Scanning electron microscope (SEM) image of MF@HPB-PPy₁₀-OA evaporator at low magnification. Inset image is high-resolution SEM image of the cross-section of MF@HPB-PPy₁₀-OA skeleton, showing a uniform wrapping of the HPB-PPy₁₀-OA coating on the MF. (b) High-resolution transmission electron microscope (HR-TEM) image of HPB-PPy₁₀-OA nanosheets. (c) Energy dispersive X-ray (EDX) elemental mapping results of MF@HPB-PPy₁₀-OA. (d-f) Water contact angle behavior of MF@PPy₁₀-OA, MF@HPB-PPy₁₀-OA and MF@HPB-PPy₁₀. (g) High-resolution x-ray photoelectron spectroscopy analysis of Mo-3d on HPB-PPy₁₀-OA. (h) Cyclic compressive stress-strain curves of MF@HPB-PPy₁₀-OA (at a set strain of 75 %) and the digital photographs (inset).

obviously enhanced (Figure S3). Among them, the optimal MF@HPB-PPy₁₀-OA possesses a

water contact angle of about $106.0 \pm 2^\circ$ (Figure 2e), corresponding to a HPB loading of about 31.6 wt% (calculated as a percentage of Mo weight). In such materials, OA has a crucial influence on the hydrophobic management of their surfaces. The OA-free MF@HPB-PPy₁₀ displays a strong hydrophilicity with a contact angle of $78.0 \pm 2^\circ$ (Figure 2f). These results demonstrate the significant contribution of HPB and OA in balancing and optimizing the hydrophilic-hydrophobic interfaces of the composite material. In addition, OA also serves the function of maintaining the mechanical properties of the material. The compressive stress-strain measurements (Figure 2g) demonstrate the excellent mechanical properties of MF@HPB-PPy₁₀-OA.

After 50 cycles of compressive stress-strain measurements (Figure 2g, top, inset), it still maintains excellent and reversible elastic deformation. Moreover, MF@HPB-PPy₁₀-OA also exhibits good bendability, twistability and tailoring properties. In contrast, the elastic deformation of the OA-free MF@HPB-PPy₁₀ fails to recover after the compressive stress-strain measurements (Figure 2g, bottom, inset). During the compressive stress-strain measurements, the HPB-PPy₁₀ coating on MF@HPB-PPy₁₀ is prone to peeling. To further confirm the composition of material, its fourier transform infrared spectra (FTIR), X-ray powder diffraction (XRD) and XPS are investigated. As shown in the FTIR (Figure S4b), the characteristic absorption peaks of HPB (including ν_{P-O} : 1053.7 cm^{-1} , ν_{Mo-O} : 954.3 cm^{-1} , $\nu_{Mo-O-Mo}$: 869.5 cm^{-1} and 770.8 cm^{-1}) and PPy (including $\nu_{C=C}$: 1533.2 cm^{-1} and ν_{C-N} : 1147.1 cm^{-1}) and OA ($\nu_{C=O}$: 1703.2 cm^{-1} , ν_{CH_3} : 2922.4 cm^{-1} and ν_{CH_2} : 2850.7 cm^{-1}) all are exhibited on MF@HPB-PPy₁₀-OA, evidencing that the successful assembly of HPB, PPy and OA on MF. A survey scan of MF@HPB-PPy₁₀-OA confirms the presence of these elements (Figure S5), which is consistent with the results of EDX mapping (Figure 2c and Figure S2c). HR-XPS of the corresponding Mo-3d indicates that the Mo3d_{3/2} and Mo3d_{5/2} at 235.3 eV and 232.2 eV are split into two sets of peaks 235.4/232.4 eV and 234.4/231.3 eV, respectively, which are referred to as Mo⁶⁺ and Mo⁵⁺.^[49,50] This reduced state of Mo confirms the presence of HPB that is favorable for solar absorption and photothermal conversion.

2.2 Solar Vapour Generation under 1 Sun

Ultraviolet-visible near-infrared (UV-Vis-NIR) measurements (Figure 3a) display excellent solar absorption properties of MF@HPB-PPy_n-OA. The MF@PPy₁₀-OA has good light absorption in the spectral range of 200-2500 nm because of the PPy coverage on MF. The absorption of MF@HPB-PPy₁₀ is visibly strengthened in the Vis-NIR region when the HPB component with excellent light absorption properties in Vis-NIR is introduced. Based on the advantages of the 3D porous structure of MF@HPB-PPy₁₀-OA and the stability and homogeneity of the HPB-PPy₁₀-OA coating, MF@HPB-PPy₁₀-OA demonstrates nearly

complete light absorption (95.3%, weighted under AM 1.5G), presenting excellent photothermal conversion potential. In Figure 3b, the surface temperature of MF@HPB-PPy₁₀-OA in the dry state rapidly increases to 89.5 °C and remains stable within 3 min under 1 sun. The photothermal conversion capacity of MF@HPB-PPy₁₀-OA is obviously higher than that of MF, MF@PPy₁₀-OA and MF@HPB-PPy₁₀, which is attributed to the superiority of HPB composition (Figure S6) and the unique surface structure. When MF@HPB-PPy₁₀-OA is in the wetted state, the temperature steady-state value of surface is slightly lower than that of MF@PPy₁₀-OA and MF@HPB-PPy₁₀ (Figure 3c). Specifically, the absorbed sunlight is applied to the photothermal water evaporation, thus the lower temperature steady-state value implies stronger evaporation efficiency. The photothermal water evaporation experiments further confirm the above results. Before executing the water evaporation, MF@HPB-PPy_n-OA improves the evaporation area and the internal temperature of structure by tailoring the edges into an orthogonal prismatic table structure (Figure S7 and Figure S8c). As displayed in

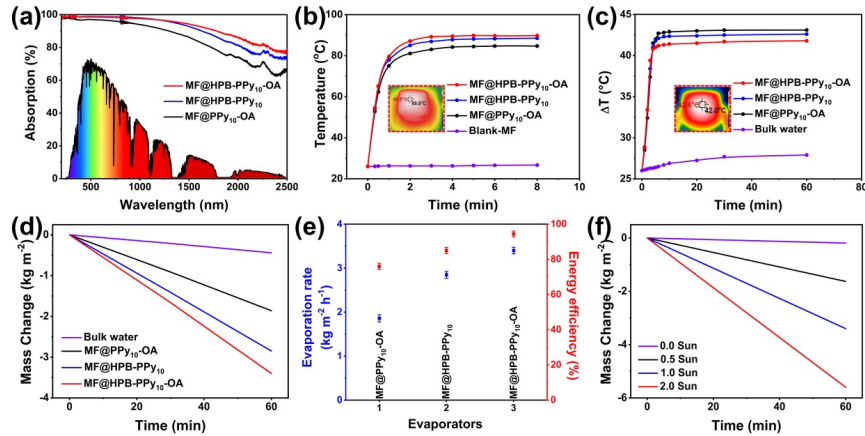


Figure 3. (a) UV-Vis-NIR spectra of MF@PPy₁₀-OA, MF@HPB-PPy₁₀, MF@HPB-PPy₁₀-OA. Inset image is the air mass 1.5 global (AM 1.5 G) solar spectrum; (b) The surface temperature rise of MF (reference), MF@PPy₁₀-OA, MF@HPB-PPy₁₀, MF@HPB-PPy₁₀-OA relative to irradiation time under 1 sun. Inset: infrared image displaying the temperature distribution after 180 s of irradiation time; (c) Plot displaying the surface temperature of bulk water (reference) and MF@PPy₁₀-OA, MF@HPB-PPy₁₀, MF@HPB-PPy₁₀-OA under 1 sun relative to irradiation time. Inset: infrared image displaying the temperature distribution after 600 s of irradiation time; (d) Mass change of MF@PPy₁₀-OA, MF@HPB-PPy₁₀, MF@HPB-PPy₁₀-OA under 1 sun illumination, with pure water as the control. And the corresponding (e) solar water evaporation rate and energy efficiency; (f) Mass change over time with MF@HPB-PPy₁₀-OA under 0 to 2 sun (0 to 2 kW m⁻²) radiation.

Figure 3d and Figure S8d, taking the bulk water as control group, the overall mass change with MF@HPB-PPy_n-OA is recorded under 1 solar irradiation. As in some previous studies, a light cut-off device with an aperture was placed between the lamp and the evaporator to ensure the same size of light irradiation and evaporator area.^[51] The general agreement of the bulk water evaporation rate value (0.43 kg m⁻²h⁻¹) under this condition with the reported literature values supports the reliability of this test system.^[9,22,52-57] Evaporation rates of 1.9 kg m⁻² h⁻¹ and 2.9 kg m⁻² h⁻¹ were obtained for the evaporation systems driven by the hydrophobic MF@PPy₁₀-OA and hydrophilic MF@HPB-PPy₁₀, respectively (Figure 3d). Compared with MF@PPy₁₀-OA, the significant increase in evaporation rate of MF@HPB-PPy₁₀ proves the positive contribution of hydrophilic HPB to the overall evaporation performance. When the interfacial hydrophilic-hydrophobicity of the materials is further modulated, MF@HPB-PPy₁₀-OA presents optimal performance with 3.4 kg m⁻² h⁻¹ evaporation rate (Figure 3d and Figure S8e), which ranks among the highest levels reported in recent years (Figure S8f).^[9,17,22,30,52-57] This is attributed to the ability of the HPB-PPy₁₀-OA self-assembled coating to wrap the MF in a more stable and uniform manner, thus presenting excellent light absorption and photothermal response. On the other hand, the small and uniformly dispersed HPB clusters of the self-assembled HPB-PPy₁₀-OA allow more hydrophilic evaporation sites to be exposed compared to HPB-PPy₁₀ (Figure 2b and Figure S2a). The excellent evaporative property of MF@HPB-PPy₁₀-OA exceeding the theoretical limit value (1.47 kg m⁻² h⁻¹) should be contributed to the active intermediate state of water molecules in the hydrophilic region. The active intermediate water which is a state intermediate between bound and free water is generally referred to as activated water.^[22,23,30] With its subtle interactions between hydrophilic sites and adjacent water molecules, the vaporization process of activated water consumes less energy than that of bulk water. It is well known that POM has good affinity for water molecules by virtue of its oxygen-rich surface structure and high negative charge.^[47,48] As shown by thermogravimetric analysis (TG) (Figure S10), the water molecules in the crystal structure of PMA evolve gradually in three stages. It is noteworthy that in the first weight loss step, the free crystalline water evolves with increasing temperature and endothermic peak 1 emerges at a low temperature of 71.9 °C in the corresponding DSC curve (while the endothermic peak of bulk water is around 100°C). The computational analysis indicates that the evolution of crystalline water in pure POM (850.0 J g⁻¹) requires only low energy compared to bulk water (2327.5 J g⁻¹, see Figure S11 in Supporting Information for details), confirming the active water molecule intermediate state in the POM structure. In the DSC analysis of Figure S11, water in MF@HPB-PPy₁₀-OA similarly proceeds with low energy consumption, indicating the activation process of water on the hydrophilic region of HPB. The equivalent dark evaporation measurements (Figure S13) results basically coincide with the DSC test results, which supports this low-energy requirement evaporation process. The energy efficiency (η) of the SVG in this system can be calculated using the following equation:

$$= h/C_{\text{opt}}P_0$$

where, \dot{m} is the water net evaporation rate (light- dark kg m⁻² h⁻¹), h is the evaporation enthalpy (J g⁻¹) of the water in MF@HPB-PPy₁₀-OA, C_{opt} is the optical concentration on the evaporator surface, P_0 is the solar radiation power (1 kW m⁻²). Thus, the energy conversion efficiency of MF@HPB-PPy₁₀-OA reaches 94.9% under 1 solar illumination (Figure 3e), obviously higher than that of MF@PPy₁₀-OA (76.0%) and MF@HPB-PPy₁₀ (88.2%). Meanwhile, the evaporation system is found to have only a low heat loss in the energy loss assessment (see Section 4.4 in Supporting Information for details). In addition, 3D MF@HPB-

PPy₁₀-OA yields a satisfactory evaporation rate of 5.6 kg m⁻² h⁻¹ with 2 solar irradiations by virtue of its unique structure (Figure 3f).

Salt -water separation in highly concentrated brine(10 wt%)

It is worthwhile to mention that MF@HPB-PPy₁₀-OA is equally efficient in high salinity brine (10 wt%), and even accomplishes complete salt-water separation. As shown in Figure 4a and Figure 4b, an inexpensive filter paper diffusion layer (with a dimensional radius 0.2 cm larger than that of MF@HPB-PPy₁₀-OA) is introduced on the basis of the conventional photothermal water evaporation system (including a light absorber layer, insulation layer and delivery line) to reinforce the transport of brine in MF@HPB-PPy₁₀-OA. In the complete salt-water separation, the average water evaporation rate of MF@PPy₁₀-OA is maintained at 1.8 kg m⁻² h⁻¹ in the optimized evaporation system, which is only slightly lower than that of bulk water (Figure 4c). Owing to the strong hydrophobicity of the MF@PPy₁₀-OA surface, salt starts to crystallize in the diffusion layer instead of at the surface during up to 32 h of continuous operation (Figure S14a). Eventually, a salt harvesting efficiency of about 88.7% is obtained around the diffusion layer. Unfortunately, after two cycles of salt-water separation, the MF@PPy₁₀-OA becomes significantly lighter in color and has a significantly lower photothermal water evaporation efficiency, which is assigned to the photobleaching effect of PPy. When MF@HPB-PPy₁₀ drives solar salt-water separation, the average rate is improved. But the salt tolerance is visibly reduced compared to that of MF@PPy₁₀-OA (Figure 4c). Due to the continuous evaporation of water, the brine concentration in the system gradually increases and approaches saturation, inevitably leading to the gradual precipitation of salt on

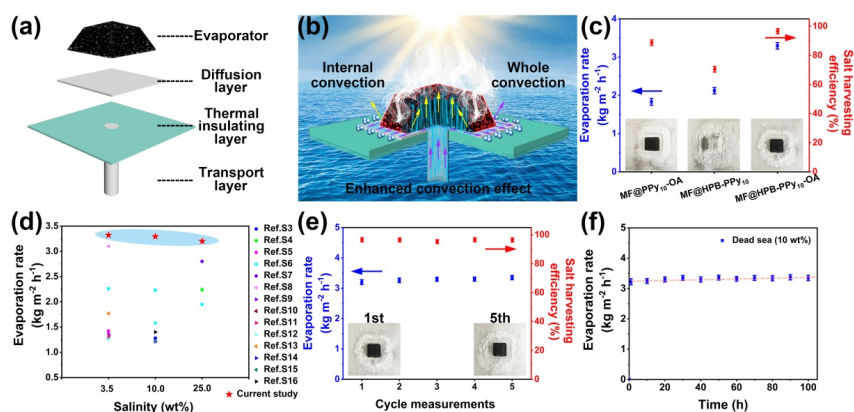


Figure 4. (a) Schematic illustration of the improved solar salt-water separation system, which consists of a rhogonal prismatic table structure MF@HPB-PPy₁₀-OA, a filter paper diffusion layer, a polystyrene foam insulation layer and a cotton swab brine transport line. The radius of the filter paper diffusion layer is 0.2 cm larger than that of the MF@HPB-PPy₁₀-OA evaporator; (b) Salt-water convection including the evaporator interior and the whole system is enhanced by combining the unique hydrophilic nano-channels of the 3D evaporator surface and the original macroporous structure as well as the size effect of the diffusion layer, achieving improved anti-salt fouling performance; (c) Water evaporation rate and salt harvesting efficiency of the evaporators in salt-water separation for high salinity sample (10 wt%). Insets correspond to digital photographs of the respective salt-water separation final results; (d) Photothermal water evaporation performance of the evaporator at wide range of salinities compared to recent literature reports. Circles and triangles refer to the reports of salt local crystallization and PPy-based evaporators, respectively; MF@HPB-PPy₁₀-OA executes (e) cycles of salt-water separation and (f) up to 100 h photothermal water evaporation measurements for high salinity brine samples.

the hydrophilic surface. It is satisfactory that MF@HPB-PPy₁₀-OA exhibits excellent photothermal water evaporation and salt-water separation capabilities. Under the identical conditions, its evaporation rate and

salt harvesting efficiency are up to $3.3 \text{ kg m}^{-2} \text{ h}^{-1}$ and 96.5% (Figure 4c and Figure S15), respectively, which belongs to the record-high of high-salinity or local salt crystallization systems reported so far and reaches zero liquid discharge. Simultaneously, the MF@HPB-PPy₁₀-OA is quite stable and maintains the high levels of evaporation rate and salt harvesting efficiency even after 5 consecutive cycles of salt-water separation demonstrated in Figure 4e, Figure S16 and Figure S17. Continuous operation for up to 100 h in 10 wt% brine that reveals stable evaporation efficiency and the ability to self-

clean in real time further confirms the outstanding of MF@HPB-PPy₁₀-OA (Figure 4f).

Such outstanding water evaporation, salt-water separation performance and continuous operation capability for high salinity brine derives primarily from the contribution of the unique structure and the hydrophilic-hydrophobic engineering of MF@HPB-PPy₁₀-OA surface. For one, the nano water channels and the photothermal active site HPB in the hydrophilic regions guarantee the excellent water transport and high-efficiency water evaporation performance at the interface. On the other hand, the OA molecular region imparts excellent real-time self-cleaning ability to the whole porous 3D structure by significantly improving the hydrophobicity of the surface, effectively suppressing the salt crystallization on surface (Figure 4c and Figure S18). Besides, according to the Hagen-Poiseuille law, the hydraulic conductivity of micropores is 10^{12} times higher than that from nano channels. The salt concentration in the nanoscale water channels of hydrophilic regions is effectively diluted by the rapid salt-water convection with the original macroporous water transport channels, resembling a "drilling effect",^[58] which boosts the anti-salt fouling performance. Benefit from the self-assembly of HPB, OA and PPy, MF@HPB-PPy₁₀-OA is characterized by excellent photothermal stability in high-salinity salt-water separation. This may be attributed to the unique function of excited state electron transfer between HPB and PPy, which substantially inhibits the photobleaching of PPy and the photo-oxidation of HPB. It is worth mentioning that the above mentioned brine convection effect is reinforced in the modified evaporation system by an innovative technology, i.e. the diffusion layer size effect. The slightly larger size of the hydrophilic filter paper diffusion layer accelerates the brine exchange between it and the 3D porous MF@HPB-PPy₁₀-OA, altering the radial concentration gradient of salt in the evaporation system and allowing the salt to preferentially crystallize at the periphery of the farthest diffusion layer (See Figure 4b, Figure S19 and Discussion section for details). The appreciable convective effect ensures the rapid diffusion and transport of brine in the MF@HPB-PPy₁₀-OA, and suppresses the crystalline precipitation of salt on the surface to some extent.^[9,52,59-60]

2.4 Laboratory and Outdoor Solar Desalination Performance

To evaluate water purification effect of MF@HPB-PPy₁₀-OA in a practical application state, a practical photothermal water evaporation system consisting of MF@HPB-PPy₁₀-OA with dimensions of $30 \times 30 \times 0.5 \text{ cm}$ under natural sunlight is meticulously monitored at the athletic field of Northeast Normal University (NENU: longitude: 125.3 E, latitude: 43.9 N) on July 11, 2022 (Figure 5a-5c). As shown in Figure 5d, the system collects up to 1.8 L of purified water in 12 h, even in a remote area with low sunlight intensity (daily average

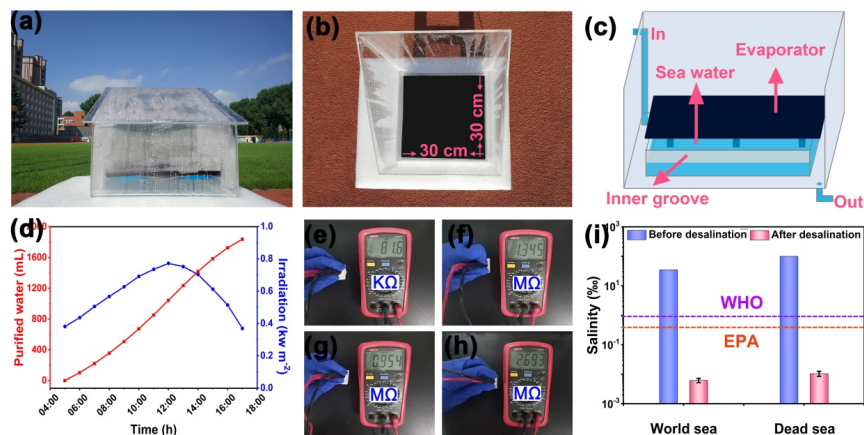


Figure 5. Solar-powered water purification equipment based on MF@HPB-PPy₁₀-OA in realistic outdoor environment. (a) Lateral view, (b) top view (photo credit: Chun Chang, NENU) and (c) internal construction view. (d) Real-time monitoring of SVG data from 5:00 to 17:00. Purity measurements by using a multimeter: (e) world sea, (f) purified water, (g) drinking water (from the water purifier supply system of NENU) and (h) ultrapure water. (i) Salinity of two simulated seawater samples (3.5 wt% and 10.0 wt%) before and after purification based on MF@HPB-PPy₁₀-OA.

intensity of about 0.61 kw m^{-2}), which is sufficient to meet the average daily drinking water demand of an adult. Impedance measurements are conducted by multimeter to evaluate the electrolyte concentration and purity of the purified water. In Figure 5e-5h, the water purification effect is outstanding and the water quality is markedly superior to the drinking water supplied by daily water purifier and well above that of seawater. After desalination, the salinities of water in samples (3.5 wt% and 10 wt% salinity) are all below the WHO and EPA (World Health Organization and US Environmental Protection Agency) drinking water quality standards by 1 to 2 orders of magnitude. The major ions, such as Na^+ , Mg^{2+} , K^+ and Ca^{2+} , are decreased in concentration by 3-4 orders of magnitude compared to seawater (Figure S20). This system can also be applied to the purification of industrial wastewater containing heavy metals or dyes (Figure S21a and Figure S21b), where the concentration of pollutants in the purified water is also reduced greatly and meets the discharge standards. These outstanding purification results demonstrate the great potential of MF@HPB-PPy₁₀-OA for practical photothermal seawater desalination and wastewater purification. Furthermore, the advantages of MF@HPB-PPy₁₀-OA in terms of mechanical properties, applicability and fabrication process (simple, low-cost and batch fabrication) allow for facile scale-up in commercialization (2.7 USD m^{-2} , see section 2.2 synthesis for details).

3. Conclusion

In conclusion, a new type of functional photothermal materials (MF@HPB-PPy_n-OA) with controllable interfacial hydrophilicity-hydrophobicity are successfully designed and obtained by the self-assembly of HPB, OA and PPy on the 3D porous MF surface for high-efficiency water evaporation and complete salt-water separation of high-salinity samples. By virtue of the unique spatial separation structure of the hydrophilic region HPB and hydrophobic region OA, the hydrophilic-hydrophobic interface of the 3D porous SVG materials is managed for the first time to balance the contradiction between efficient water evaporation and salt crystallization. Meanwhile, the strong brine convection effect formed between the nano-water channels on the hydrophilic region and the microporous channels of MF@HPB-PPy_n-OA further enhances the anti-salt fouling performance. Among them, MF@HPB-PPy₁₀-OA can operate continuously and stably for over 100 h at ultrahigh evaporation rate of $3.3 \text{ kg m}^{-2} \text{ h}^{-1}$ under 1 sun while surface free of salt crystallization for desalination of high-salinity brine (10 wt%). More notably, MF@HPB-PPy₁₀-OA accomplishes the com-

plete salt-water separation of 10 wt% brine, yielding up to 3.3 kg m⁻² h⁻¹ and 96.5% evaporation rate and salt harvesting efficiency, which realizes a record-high for high salinity or local salt crystallization systems. Apart from the high-efficiency performance, MF@HPB-PPy₁₀-OA also holds the advantages of simple process, low-cost, and batch manufacturing, indicating broad applicability in the fields of solar humidification, salt extraction from seawater and wastewater purification. This study not only demonstrates the vital role of interfacial hydrophilic-hydrophobic engineering for high-efficiency, salt-resistant and sustainable operation, but also advances the development of novel HPB-based SVG functional materials for seawater desalination and zero liquid discharge.

Supporting Information

Supporting Information is available from the Wiley Online Library or from the author.

Acknowledgements

S. H. Cheng. and C. M. Liu. contributed equally to this work. This work is financially supported by the National Key Basic Research Program of China (grant no. 2020YFA0406101), National Natural Science Foundation of China (grant nos. 22071020, 22171041, 21901035, 22271043), Natural Science Foundation of Jilin Province Science and Technology Department (grant no. 20220101045JC), the Fundamental Research Funds for the Central Universities (grant nos. 2412021QD008).

Conflict of Interest

The authors declare no conflict of interest.

Received: ((will be filled in by the editorial staff))

Revised: ((will be filled in by the editorial staff))

Published online: ((will be filled in by the editorial staff))

References

- [1] C. J. Vörösmarty, P. Green, J. Salisbury, R. B. Lammers, *Science* **2000** , 289 , 284.
- [2] T. A. Larsen, S. Hoffmann, C. LüthiB, Truffer, M. Maurer, *Science* **2016** , 352 , 928.
- [3] C. Y. He, Z. F. Liu, J. G. Wu, X. H. Pan, Z. H. Fang, J. W. Li, B. A. Bryan, *Nat Commun* **2021** , 12 , 4667.
- [4] S. F. Singer, *Science* **1970** , 168 , 1286.
- [5] M. Elimelech, W. A. Phillip, *Science* **2011** , 333 , 712.
- [6] P. E. Glaser, *Science* **1965** , 148 , 1127.
- [7] N. Xu, J. L. Li, Y. Wang, C. Fang, X. Q. Li, Y. X. Wang, L. Zhou, B. Zhu, Z. Wu, S. N. Zhu, J. Zhu, *Sci Adv* **2019** , 5 , eaaw7013.
- [8] Z. X. Wang, T. Horseman, A. P. Straub, N. Y. Yip, D. Y. Li, M. Elimelech, S. H. Lin, *Sci Adv* **2019** , 5 , eaax0763.
- [9] L. Wu, Z. C. Dong, Z. R. Cai, T. Ganapathy, N. X. Fang, C. X. Li, C. L. Yu, Y. Zhang, Y. L. Song, *Nat Commun* **2020** , 11 , 521.
- [10] W. X. Guan, Y. H. Guo, G. H. Yu, *Small* **2021** , 17 , e2007176.
- [11] F. Nawaz, Y. W. Yang, S. H. Zhao, M. H. Sheng, C. Pan, W. X. Que, *J. Mater. Chem. A* **2021** , 9 , 16233.
- [12] L. N. Zhang, X. Y. Li, Y. Zhong, A. Leroy, Z. Y. Xu, L. Zhao, E. N. Wang, *Nat Commun* **2022** , 13 , 849.

- [13] C. L. Zhang, Y. Shi, L. Shi, H. X. Li, R. Y. Li, S. Hong, S. F. Zhuo, T. J. Zhang, P. Wang, *Nat Commun* **2021** , *12* , 998.
- [14] K. J. Yang, T. T. Pan, S. C. Dang, Q. Q. Gan, Y. Han, *Nat Commun* **2022** , *13* , 6653.
- [15] M. Miyazaki, A. Fujii, T. Ebata, N. Mikami, *Science***2004** , *304* , 1134.
- [16] A. Fujii, K. Mizuse, *Int. Rev. Phys. Chem.***2013** , *32* , 266.
- [17] F. Z. Zhao, X. Y. Zhou, Y. Shi, X. Qian, M. Alexander, X. P. Zhao, S. Mendez, R. G. Yang, L. T. Qu, G. H. Yu, *Nature Nanotechnology* **2018** , *13* , 489.
- [18] Q. C. Lu, W. X. Shi, H. Z. Yang, X. Wang, *Adv. Mater.***2020** , *32* , e2001544.
- [19] Y. Zhou, Q. C. Lu, Q. D. Liu, H. Z. Yang, J. L. Liu, J. Zhuang, W. X. Shi, X. Wang, *Adv. Funct. Mater.* **2021** , *32* , 2112159.
- [20] F. Zhao, Y. H. Guo, X. Y. Zhou, W. Shi, G. H. Yu, *Nature Reviews Materials* **2020** , *5* , 388.
- [21] J. X. Xiao, Y. Guo, W. Q. Luo, D. Wang, S. K. Zhong, Y. R. Yue, C. N. Han, R. X. Lv, J. B. Feng, J. Q. Wang, W. Huang, X. L. Tian, W. Xiao, Y. J. Shen, *Nano Energy* **2021** , *87* , 106213.
- [22] P. Liu, Y. B. Hu, X. Y. Li, L. Xu, C. Chen, B. L. Yuan, M. L. Fu, *Angew. Chem. Int. Ed. Engl.* **2022** , *61* , e202208587;
- [23] Y. H. Guo, J. Bae, Z. W. Fang, P. P. Li, F. Zhao, G. H. Yu, *Chem. Rev.* **2020** , *120* , 7642.
- [24] W. J. Tu, Z. Z. Wang, Q. Y. Wu, H. Huang, Y. Liu, M. W. Shao, B. W. Yao, Z. H. Kang, *J Mater Chem A* **2020** , *8* , 10260.
- [25] L. Zhou, Y. L. Tan, D. X. Ji, B. Zhu, P. Zhang, J. Xu, Q. Q. Gan, Z. F. Yu, J. Zhu, *Sci Adv* **2016** , *2* , e1501227.
- [26] X. Q. Li, J. L. Li, J. Y. Lu, N. Xu, C. L. Chen, X. Z. Min, B. Zhu, H. X. Li, L. Zhou, S. N. Zhu, T. J. Zhang, J. Zhu, *Joule***2018** , *2* , 1331.
- [27] W. C. Xu, X. Z. Hu, S. D. Zhuang, Y. X. Wang, X. Q. Li, L. Zhou, S. N. Zhu, J. Zhu, *Adv Energy Mater* **2018** , *8* , 1702884.
- [28] Y. W. Yang, H. Y. Zhao, Z. Y. Yin, J. Q. Zhao, X. T. Yin, N. Li, D. D. Yin, Y. N. Li, B. Lei, Y. P. Du, W. X. Que, *Mater Horiz***2018** , *5* , 1143.
- [29] R. Hu, J. Q. Zhang, Y. D. Kuang, K. B. Wang, X. Y. Cai, Z. Q. Fang, W. Q. Huang, G. Chen, Z. X. Wang, *J Mater Chem A***2019** , *7* , 15333.
- [30] Y. H. Guo, X. Zhao, F. Zhao, Z. H. Jiao, X. Y. Zhou, G. H. Yu, *Energy & Environmental Science* **2020** , *13* , 2087.
- [31] H. Y. Zhao, J. Zhou, Z. L. Yu, L. F. Chen, H. J. Zhan, H. W. Zhu, J. Huang, L. A. Shi, S. H. Yu, *Cell Reports Physical Science***2020** , *1* , 100074.
- [32] Y. Q. Zhu, G. L. Tian, Y. W. Liu, H. X. Li, P. C. Zhang, L. Zhan, R. Gao, C. Huang, *Adv Sci* **2021** , *8* , e2101727.
- [33] S. S. Wang, G. Y. Yang, *Chem. Rev.* **2015** , *115* , 4893.
- [34] L. C. Baker, D. C. Glick, *Chem. Rev.* **1998** , *98* , 3.
- [35] D. L. Long, E. Burkholder, L. Cronin, *Chem. Soc. Rev.***2007** , *36* , 105.
- [36] L. Chen, W. L. Chen, X. L. Wang, Y. G. Li, Z. M. Su, E. B. Wang, *Chem. Soc. Rev.* **2019** , *48* , 260.
- [37] J. W. Zhang, Y. C. Huang, G. Li, Y. Wei, *Coord. Chem. Rev.* **2019** , *378* , 395.

- [38] M. D. Symes, L. Cronin, *Nat Chem* **2013** ,5 , 403.
- [39] Q. W. Yan, W. D. Yu, J. Yan, *Chin. Sci. Bull.***2018** , 63 , 3296.
- [40] X. F. Chen, G. H. Zhang, B. Li, L. X. Wu, *Sci Adv***2021** , 7 , eabf8413.
- [41] Z. Fang, Z. Deng, X. Y. Wan, Z. Y. Li, X. Ma, S. Hussain, Z. Z. Ye, X. S. Peng, *Applied Catalysis B: Environmental* **2021** ,296 , 120329.
- [42] A. Bijelic, M. Aureliano, A. Rompel, *Angew. Chem. Int. Ed. Engl.* **2019** , 58 , 2980.
- [43] G. Guedes, S. Q. Wang, F. Fontana, P. Figueiredo, J. Lindén, A. Correia, R. J. B. Pinto, S. Hietala, F. L. Sousa, H. A. Santos, *Adv. Mater.* **2021** , 33 , e2007761.
- [44] F. Khan, Y. Jang, Y. Patil, R. Misra, F. D'Souza, *Angew. Chem. Int. Ed. Engl.* **2021** , 60 , 20518.
- [45] C. Zhang, W. B. Bu, D. L. Ni, C. J. Zuo, C. Cheng, Q. Li, L. L. Zhang, Z. Wang, J. L. Shi, *J. Am. Chem. Soc.* **2016** ,138 , 8156.
- [46] Z. Yang, W. P. Fan, W. Tang, Z. Y. Shen, Y. L. Dai, J. B. Song, Z. T. Wang, Y. Liu, L. Lin, L. L. Shan, Y. J. Liu, O. Jacobson, P. F. Rong, W. Wang, X. Y. Chen, *Angew. Chem. Int. Ed. Engl.***2018** , 57 , 14101.
- [47] X. E. Cai, D. C. Du, J. P. Ni, Y. M. Jin, J. Zhu, Y. X. Qian, *Thermochim. Acta* **1997** , 292 , 45.
- [48] F. K. Ahmadabad, M. Pourayoubi, H. Bakhshi, *Mater. Chem. Phys.* **2017** , 199 , 79.
- [49] H. F. Shi, G. Yan, Y. Zhang, H. Q. Tan, W. Z. Zhou, Y. Y. Ma, Y. G. Li, W. L. Chen, E. B. Wang, *ACS Appl Mater Interfaces***2017** , 9 , 422.
- [50] H. F. Shi, Y. C. Yu, Y. Zhang, X. J. Feng, X. Y. Zhao, H. Q. Tan, S. U. Khan, Y. G. Li, E. B. Wang, *Applied Catalysis B: Environmental* **2018** , 221 , 280.
- [51] X. Q. Li, G. Ni, T. Cooper, N. Xu, J. L. Li, L. Zhou, X. Z. Hu, B. Zhu, P. C. Yao, J. Zhu, *Joule* **2019** , 3, 1798.
- [52] H. Y. Geng, Q. Xu, M. M. Wu, H. Y. Ma, P. P. Zhang, T. T. Gao, L. T. Qu, T. B. Ma, C. Li, *Nat Commun* **2019** , 10 , 1512.
- [53] X. J. Liu, Y. P. Tian, F. Q. Chen, A. Caratenuto, J. A. DeGiorgis, M. ELSonbaty, Y. S. Wan, R. Ahlgren, Y. Zheng, *Adv. Funct. Mater.* **2021** , 31 , 2100911.
- [54] L. Zhu, L. Sun, H. Zhang, H. Aslan, Y. Sun, Y. D. Huang, F. Rosei, M. Yu, *Energy & Environmental Science* **2021** ,14 , 2451.
- [55] Y. J. Hu, H. Y. Ma, M. M. Wu, T. Y. Lin, H. Z. Yao, F. Liu, H. H. Cheng, L. T. Qu, *Nat Commun* **2022** , 13 , 4335.
- [56] X. H. Liu, F. X. Chen, Y. K. Li, H. J. Jiang, D. D. Mishra, F. Yu, Z. H. Chen, C. Q. Hu, Y. Chen, L. T. Qu, W. T. Zheng, *Adv. Mater.* **2022** , 34 , e2203137.
- [57] W. Zhou, C. L. Zhou, C. F. Deng, L. Chen, X. J. Zeng, Y. X. Zhang, L. X. Tan, B. S. Hu, S. Guo, L. C. Dong, S. C. Tan, *Adv. Funct. Mater.* **2022** , 32 , 2113264.
- [58] Y. D. Kuang, C. J. Chen, S. M. He, E. M. Hitz, Y. L. Wang, W. T. Gan, R. Y. Mi, L. B. Hu, *Adv. Mater.* **2019** , 31 , e1900498.
- [59] Y. Xia, Q. F. Hou, H. Jubaer, Y. Li, Y. Kang, S. Yuan, H. Y. Liu, M. W. Woo, L. Zhang, L. Gao, H. T. Wang, X. W. Zhang, *Energy & Environmental Science* **2019** , 12 , 1840.
- [60] L. Li, N. He, B. Jiang, K. W. Yu, Q. Zhang, H. T. Zhang, D. W. Tang, Y. C. Song, *Adv. Funct. Mater.* **2021** , 31 , 2104380.

The self-assembly of heteropoly blue (HPB), oleic acid (OA) and polypyrrole (PPy) on 3D porous melamine foam (MF) achieves a new type of hydrophilic-hydrophobic composite interfacial materials MF@HPB-PPy_n-OA, which exhibit high-efficiency water evaporation and salt harvesting in salt-water separation at high-salinity (10 wt%).

Keywords: polyoxometalates (POM), heteropoly blue (HPB), hydrophilic-hydrophobic interface, solar vapour generation (SVG), salt-water separation

Sihang Cheng, Cuimei Liu, Yingqi Li, huaqiao Tan*, Yonghui Wang, Yangguang Li*

Polyoxometalates-Modulated Hydrophilic-Hydrophobic Composite Interfacial Material for Efficient Solar Water Evaporation and Salt Harvesting in High Salinity Brine

TOC figure

